RSC Advances

PAPER

View Article Online
View Journal | View Issue

Cite this: *RSC Adv.*, 2024, **14**, 10358

Bimetallic Co–Mn catalysts for synergistic enhancement of VOC gas-sensing performance of ZnO hierarchical nanostructures

Yuwei Qu and Jun Zhang *

The synergistic effect between bonding dissimilar metals is a very effective way to improve the performance of metal catalysts. In this work, we prepared a series of bimetallic co-doped ZnO hierarchical nanostructures by controlling Mn and Co contents. The gas-sensing properties of the sensors based on the bimetallic co-doped ZnO hierarchical nanostructures were studied systematically through different volatile organic compound (VOC) vapors for the temperature range from 160 to 400 °C. In the testing of normal butanol gas by the bimetallic co-doped ZnO sensor, its performance was tens of times higher than that of pure zinc oxide, and the response values to other VOCs tested were very low, which also indicates that the sensor has good selectivity. The promoted performance is attributed to the increase of adsorbed oxygen content on the surface of the sensor material due to the bimetallic synergistic enhancement effect. XPS spectra of O 1s region of the sensor show that the adsorbed oxygen content is 22.4%, which is higher than that of the pure ZnO (8.5%). The synergistic effect between bimetallic Mn and Co leads to electron enrichment on the surface of ZnO. Electron enrichment can not only promote the activation of ZnO, but also can help to improve the gas-sensing performance.

Received 22nd January 2024
Accepted 19th March 2024

DOI: 10.1039/d4ra00553h

rsc.li/rsc-advances

1. Introduction

At ambient temperature, a group of chemical compounds referred to as volatile organic compounds (VOCs) readily undergo evaporation.[1] Not only are they detrimental to the environment, but they also pose significant risks to people's safety and well-being. For instance, normal butanol, a vital solvent and raw material for organic synthesis, is commonly used in industrial settings and laboratories. However, when normal butanol enters the human body, it can lead to poisoning, with symptoms including dizziness, fatigue, nausea, vomiting, headaches, and irritability.[2] In severe cases, it may even result in coma, cramps, and respiratory failure. Furthermore, prolonged exposure to normal butanol can lead to health issues such as liver and lung damage. Regarding the maximum allowable concentration of butanol in the air, different countries may have different regulations and standards. For example, the U.S. Vocational Safety and Health Administration (OSHA) sets the acceptable exposure limit (PEL) for 1-butanol to the time weighted average (TWA) of 100 ppm (300 mg m^{-3}). The exposure limit (REL) recommended by Niosh is the upper limit of 50 ppm (150 mg m^{-3}). These values are usually used to guide chemical management and control measures in industrial and professional environments to ensure the safety of workers.

Due to their ease of modification, high specific surface area, and exceptional photoelectric properties, ZnO nanomaterials have found extensive applications in catalysts, ceramics, rubber, optoelectronic devices, and various other fields, establishing themselves as one of the most promising oxide semiconductors, thereby garnering considerable attention.[3,4] Additionally, their prospects in sensor applications are incredibly vast, owing to their wide band gap, remarkable response to gas detection, rapid response rate, cost-effectiveness, and other advantageous attributes.[5–7]

The response and selectivity of single-component ZnO gas sensors still require further enhancement. Doping with metal or non-metal ions is a common approach to improve the gas response of single-component ZnO.[8] It has been demonstrated that element doping can modify ZnO's band gap width and crystal structure, a crucial means to enhance the material's functionality. ZnO is particularly well-suited for doping with main group metal or transition metal ions since Zn^{2+} and O^{2-} predominantly exist in an ionic state in ZnO.[9,10] The addition of magnetic elements such as Co, Mn, Ni, and others to ZnO has been shown to enhance the material's photoelectric characteristics.[11–14] The synergistic effect between bonding different metals is a very effective way to improve the performance of sensors. However, it is very difficult to achieve synergy between two metals with different properties. In this study, a series of bimetallic (Mn, Co) co-doped ZnO hierarchical nanostructures by different Mn and Co contents were synthesized through CVD method. The photo-electronic and gas-

School of Physics & Electronic Information, Yantai University, Yantai 264005, P.R. China. E-mail: jzhang@ytu.edu.cn

sensing properties of the resulting (Co, Mn) co-doped ZnO hierarchical nanostructures will be thoroughly investigated. The promoted gas-sensing performance mechanism would be attributed to bimetallic synergistic enhancement effect. Further, the adsorption oxygen content of O 1s fractional peak in XPS spectra further confirmed that the synergistic effect between bonding bimetallic Co and Mn can enrich electrons on the surface of ZnO and improve the gas-sensing performance of ZnO hierarchical nanostructures.

2. Experimental

2.1 Synthesis of (Co, Mn) co-doped ZnO hierarchical nanostructures

Chemical vapor deposition (CVD) was used to prepare bimetallic (Co, Mn) co-doped ZnO hierarchical nanostructure. Weigh a specific quantity of pure Zn powder along with $C_4H_6CoO_4 \cdot 4H_2O$, $C_4H_6MnO_4 \cdot 4H_2O$, and C powder. The above reagents are produced by Tianjin Huasheng Chemical Reagent Co., Ltd. in China. Ensure that the mass ratios of pure Zn powder to $C_4H_6CoO_4 \cdot 4H_2O$, $C_4H_6MnO_4 \cdot 4H_2O$, and C powder are as well as in order, 1 : 3% : 5% : 50%, 1 : 5% : 5% : 50%, 1 : 7% : 5%: 50%, and 1 : 9% : 5% : 50%. We weigh out 1 g of ZnO and continue to weigh other samples based on this mass ratio. Mix well after carefully grinding in an agate mortar. Put the combined ingredients in a ceramic vessel and warm them in the heart of a high-temperature tube furnace. The temperature within the high-temperature tube furnace is quickly increased to 760 °C and then maintained there for 120 minutes using a temperature management system. The system is free cooling to room temperature after heating. The experiments should be repeated under identical conditions, and the results of the various ZnO samples with different Co and Mn dopant ratios mentioned above should be correspondingly labeled as ZC1, ZC2, ZC3, and ZC4, respectively. In addition, under the same experimental conditions, the pure ZnO nanostructures is named ZC0. The acquired samples were then each individually characterized.

2.2 Characterizations of (Co, Mn) co-doped ZnO hierarchical nanostructures

The crystal structures of ZC0, ZC1, ZC2, ZC3, and ZC4 were measured by an X-ray diffraction (XRD; Ultima IV, Rigaku, Japan) with a Cu Kα radiation operated at 40 kV and 40 mA in the 2θ region of 30–70° at a scan rate of 10°/min. The surface morphology and structure of the nanomaterials were observed using scanning electron microscopy (SEM, JEOL JSM-5610LV). (Co, Mn) co-doped ZnO hierarchical nanostructures were identified using X-ray photoelectron spectroscopy (XPS; Escalab 250 Xi, Thermo Scientific) to analyze the matrix's chemical make-up. Using the Edinburgh FLS920 fluorescence spectrometer, the sample was excited by a 325 nm He Cd laser light source, and the Photoluminescence (PL) spectra obtained were used to detect the structural characteristics and physical properties of the samples.

2.3 Fabrication and testing of normal butanol gas sensors based on (Co, Mn) co-doped ZnO hierarchical nanostructures

Firstly, the prepared (Co, Mn) co-doped ZnO nanostructures and pure ZnO nanomaterials were thoroughly ground in an agate mortar and mixed with anhydrous ethanol to form a suspension. Subsequently, the freshly prepared suspension was uniformly coated onto the surface of a flat ceramic substrate. Finally, the sensors were placed in a high-temperature tube furnace and heated at 150 °C for 300 minutes to facilitate the evaporation of the anhydrous ethanol from the material surface and to induce sample aging.

The gas sensors were tested using the static gas allocation method. A certain volume of *n*-butanol was extracted using a syringe and evaporated into gas in the evaporator. The sensors made under a working voltage of 2.0 V were then exposed to *n*-butanol, and the resistance change was measured. The response of the sensors at different temperatures was calculated, and the data were recorded using a photoelectric intelligent gas comprehensive testing platform (CGS-MT, Beijing Elite Technology Company).

3. Results and discussion

As shown in Fig. 1(a)–(e), the phase components of the samples (ZC1, ZC2, ZC3, ZC4, and ZC0, respectively) were examined by XRD. Before and after doping, sharp, and strong diffraction peaks were created, showing that all samples were highly crystalline. The only crystal phase found is ZnO with hexagonal wurtzite structure, and no other crystal phases corresponding to Co and Mn or Co and Mn compounds are observed, showing that the doped Co and Mn ions are primarily integrated into the ZnO lattice.[15–18]

Using XRD data, the lattice parameter (c) of the samples (ZC1, ZC2 ZC3, ZC4, and ZC0, respectively) was estimated using the following formulae.

$$\sin^2\theta = \frac{\lambda^2}{4}\left[\frac{4}{3}\left(\frac{h^2+hk+k^2}{\alpha^2}\right)+\frac{l^2}{c^2}\right] \quad (1)$$

The wavelength of Cu K radiation (λ) is 1.541 Å; θ is the Bragg angle; h, k, and l are the Miller's indices.[19] ZC1 = 5.20609 Å, ZC2 = 5.20575 Å, ZC3 = 5.20595 Å, ZC4 = 5.20621 Å and ZC0 = 5.20565 Å are the estimated lattice parameter. Therefore, replacing Zn^{2+} with Co^{2+} and Mn^{2+} may lead to an increase in lattice parameter. The diffraction peak in the ZnO crystal cell changes somewhat when Co^{2+} and Mn^{2+} are doped, suggesting that the crystal inflation after doping.[20,21] The ionic radius of Co^{2+} and Mn^{2+} are 0.75 Å and 0.83 Å, respectively, while that of Zn^{2+} is 0.68 Å, supporting the conclusion.[22] The shift in the samples XRD spectra shows that the Co^{2+} and Mn^{2+} ions were successfully incorporated into the ZnO structure at the Zn^{2+} site.[23] Fig. 1(f) depicts the morphology of (Co, Mn) co-doped ZnO hierarchical nanostructures (ZC2) and Fig. 1(g) depicts the morphology of pure ZnO hierarchical nanostructures (ZC0).

Raman spectra of the samples (ZC1, ZC2 ZC3, ZC4, and ZC0, respectively) are shown in Fig. 2(a)–(e). These samples had

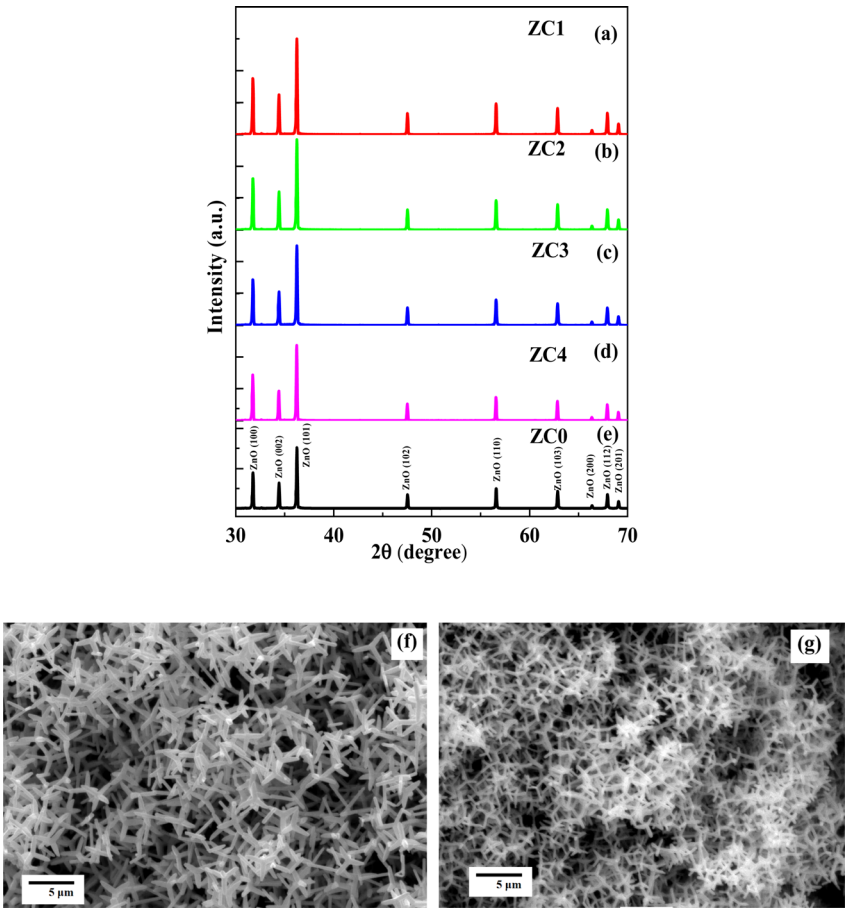

Fig. 1 (a–d) XRD patterns of the ZC1, ZC2, ZC3, and ZC4, respectively; (e) XRD patterns of pure ZnO nanostructures (ZC0). (f) SEM image of (Co, Mn) co-doped ZnO nanostructures (ZC2). (g) SEM image of pure ZnO nanostructures (ZC0).

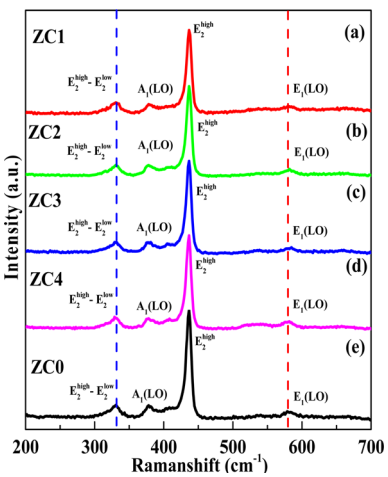

Fig. 2 (a–d) Raman spectra of the ZC1, ZC2, ZC3, and ZC4, respectively; (e) Raman spectrum of pure ZnO nanostructures (ZC0).

multi-photon Raman scattering that was observed between 200 and 700 cm $^{-1}$, respectively. According to the results in the Fig. 2(a)–(d), the four Raman characteristic peaks may be found. It is evident that the transverse optical wave (TO) of A_1 is the vibration mode at 378.1 cm $^{-1}$, the high-frequency vibration mode E_2^{high} of ZnO is the strongest vibration mode at 436.6 cm $^{-1}$, and the peaks at 330.4/328.8 cm $^{-1}$ and 584.9/581.9 cm $^{-1}$ correspond to the second order multi-phonon modes $E_2^{high} - E_2^{low}$ and E_1 (LO), respectively. The Raman spectra of pure ZnO nanostructures is shown in Fig. 2(e). A change in crystal structure will cause a shift in the peak position of the Raman spectrum.[24,25] Compared with the Raman spectrum of pure ZnO nanostructures, the mode E1 (LO) of (Co, Mn) co-doped ZnO nanostructures is red-shifted, and the $E_2^{high} - E_2^{low}$ mode is blue-shifted. This can be attributed to the expansion of the unit cell caused by the incorporation of Co ions and Mn ions into the lattice sites of Zn^{2+}. This suggests that the doping of Co and Mn into ZnO may be successful.[26]

In order to describe samples and establish the oxidation state of its constituent elements, XPS investigation from the ZC2 as example are shown in Fig. 3. XPS full scan spectrum of the ZC2 (including five elements Zn, O, C, Co, and Mn) is illustrated in Fig. 3(a). The binding energy of C 1s, the internal standard, is 284.8 eV. The high-resolution Zn 2p energy spectra from the ZC2 and ZC0 samples are depicted in Fig. 3(b), respectively. The results reveal that the spin orbit double peaks of Zn $2p_{1/2}$ and Zn $2p_{3/2}$ of the ZC2 sample have respective energies of 1021.35 eV and 1044.40 eV, and peaks of Zn $2p_{1/2}$ and Zn $2p_{3/2}$ of the ZC0

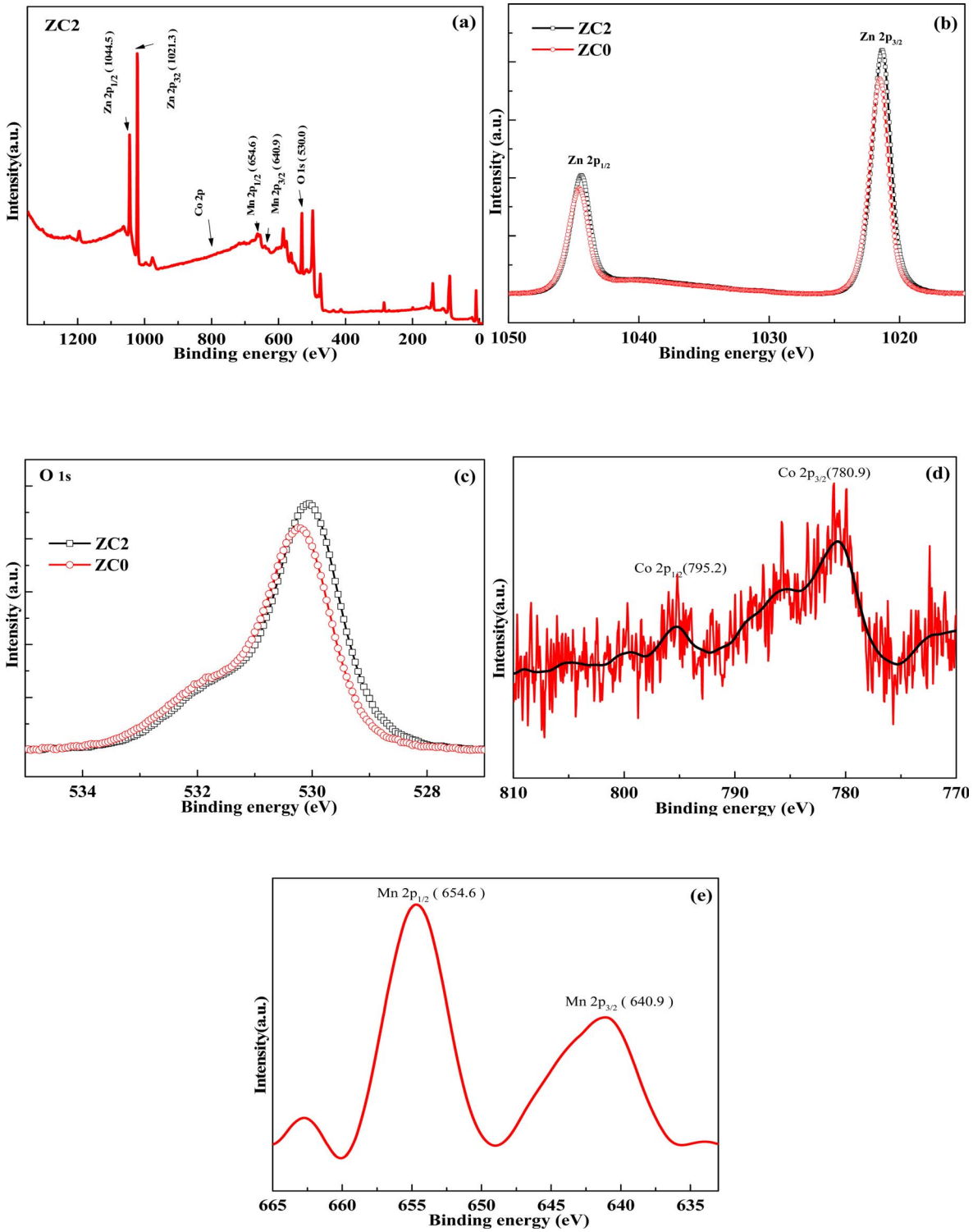

Fig. 3 (a) XPS spectra of the survey scans of the ZC2. (b) XPS spectra of Zn 2p of the ZC2 and ZC0, respectively. (c) XPS spectra of O 1s of the ZC2 and ZC0, respectively. (d) XPS spectra of Co 2p of the ZC2. (e) XPS spectra of Mn 2p of the ZC2.

sample are energies of 1021.55 eV and 1044.60 eV. This suggests that Zn is in the valence state of Zn^{2+}. The typical O 1s spectra from the ZC2 and ZC0 samples are shown in Fig. 3(c), respectively. The O 1s peak of the ZC2 is located at 530.05 eV and the O 1s peak of the ZC0 is located at 530.25 eV. The results indicate that the ZC2 has 0.20 eV shift in the direction of low binding energy compared with the ZC0. The high-resolution Co 2p energy spectrum shown in Fig. 3(d) shows the spin orbit double peaks of Co $2p_{3/2}$ and Co $2p_{1/2}$, as well as their satellite peaks. The binding energy of the spin orbit double peaks of Co $2p_{3/2}$

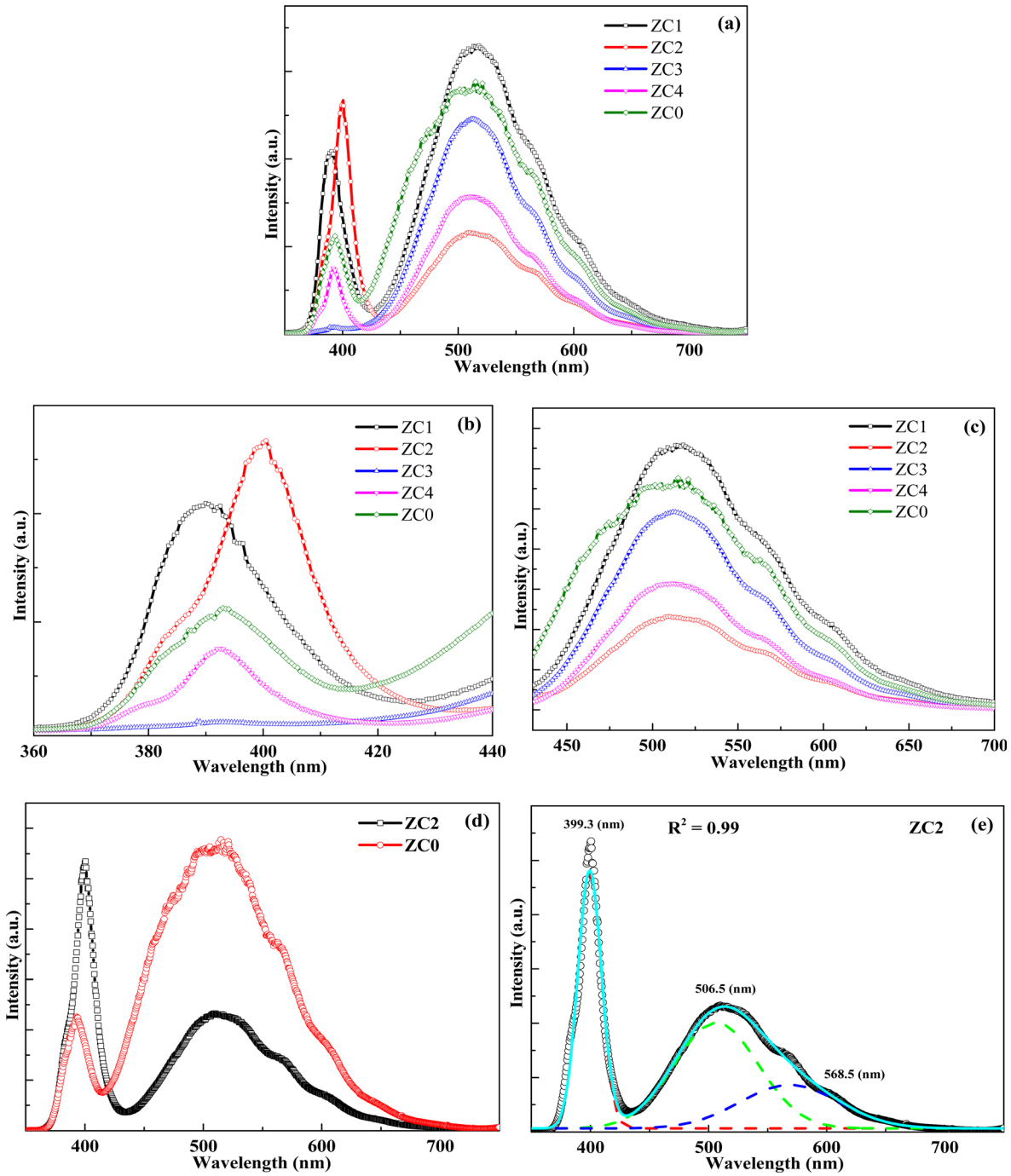

Fig. 4 (a) PL spectra of the ZC1, ZC2, ZC3, ZC4, and ZC0, respectively. (b) UV emission peaks of PL spectra of the ZC1, ZC2, ZC3, ZC4, and ZC0, respectively. (c) Deep level emission peak of PL spectra of the ZC1, ZC2, ZC3, ZC4, and ZC0, respectively. (d) PL spectra of ZC2 and ZC1, respectively. (e) Deconvolution of PL spectrum for the ZC2 sample.

and Co $2p_{1/2}$, as well as their satellite peaks, are seen in the high-resolution Co 2p energy spectrum depicted in Fig. 3(d). The two major peaks' respective binding energies are 780.9 eV and 795.2 eV. The existence of Co^{2+} is confirmed by the spin orbit splitting at 14.3 eV.[27] The high-resolution Mn 2p energy spectrum is displayed in Fig. 3(e). At 640.9 eV and 654.6 eV, respectively, two binding energy peaks corresponding to Mn $2p_{3/2}$ and Mn $2p_{1/2}$ were seen. Since the binding energies differ by 13.7 eV, the majority of Mn ions are in the Mn^{4+} valence.[28,29] The presence of mixed valence states of Mn^{3+} and Mn^{4+} is also indicated by full width at half peak (FWHM) > 3 eV.[30,31] The satellite peak, which appears at roughly 643.5 eV, is another feature of Mn^{3+}.[32] The XPS spectra demonstrated that the ZnO lattice had been doped with Co and Mn ions.

PL spectra of all samples (ZC1, ZC2, ZC3, ZC4, and ZC0, respectively) at room temperature are shown in Fig. 4(a). The

results indicate that there are an ultraviolet (UV) emission peak at 390–400 nm and a broad-strong green emission peak at 510–520 nm in all samples. The UV peak is caused by the free exciton recombination of ZnO and peak-shift occurs with different doping concentration. As shown in Fig. 4(b), with the gradual increase of Co doping concentration, the peak value of UV luminescence first shifts to red and then to blue. The main reason for this could be a change in energy band after doping Co and Mn. Co and Mn doping have been shown to effectively adjust the band gap of ZnO hierarchical nanostructures.[19,33] The green peak at 510–520 nm is brought on by various contaminants or flaws[19] and the oxygen vacancy concentration is correlated with the shift in the deep level luminescence peak as shown in Fig. 4(c). The results show that the luminescence intensity of doped samples is different, but the peak position does not shift.

In order to further study the influence of doping on emission characteristics, ZC2 and ZC0 as shown in Fig. 4(d) are selected for comparative study. The PL spectra of ZC2 and ZC0 have a strong ultraviolet mission peak at 399.3 nm, respectively. The peak shifts red by 7 nm when compared to ZC0 (pure ZnO). This is due to the sample's size, structure, material type, and other factors changing after it has been doped with Co and Mn.[34,35] The deep level emission peak of ZC2 at 510 nm is attributed to the emission of defects. The intensity of the deep level emission peak of ZC2 is significantly reduced when compared to ZC0, implying that the concentration of oxygen vacancies related to deep emission during the doping process is significantly reduced. The greater the intensity ratio of the ultraviolet emission peak to the deep level emission peak, the higher the material's crystallinity. The ZC2 has a much higher ratio than that of ZC0. It demonstrates that (Co, Mn) co-doping results in fewer defects and higher crystallinity. This could be due to the reduction of defects in the crystal caused by ZnO doping, resulting in a reduction in the intensity of the deep level emission peak and a slight blue shift. The experimental results indicate that the ZC2 sample has higher crystallinity than the ZC0 sample, has a lower carrier coincidence rate, and can promote charge transfer. To confirm this guess, we calculate the XRD data of sample ZC2 and ZC0. Crystallinity refers to the proportion of crystalline regions within a polymer material at room temperature, calculated as the ratio of the crystalline portion to the total material (crystalline portion + amorphous portion).

$$f_{\mathrm{w}}^{\mathrm{c}} = \frac{W_c}{W_c + W_a} \tag{2}$$

In the equation, W represents weight, subscript c denotes crystalline, and subscript a denotes amorphous. By calculation, the crystallinity of sample ZC2 is 71.63%, and the crystallinity of sample ZC0 is 59.59%. This indicates that the crystallinity of ZnO has increased during the doping process.

In order to detailed study of the PL emission through defects from the ZC2, the multiple peaks Gaussian fitting of the PL spectra of ZC2 are shown in Fig. 4(e). The red line's high and narrow peak at 399.3 nm represents the UV emission peak of ZC2, which is brought on by the free exciton recombination of ZnO. The deep-level emission peak, which is the broad and low peak of the green line at 505.5 nm, is brought on by flaws like oxygen vacancies. The peak of the blue line at 568.5 nm may be the result of additional flaws from Co and Mn doping ZnO.

The optoelectronic properties of the sensor based on the ZC2 under different illumination conditions: dark, 325 nm and 442 nm wavelengths of laser are shown in Fig. 5(a), respectively. The scanning voltage range at both electrode ends is (−10 V, 10 V). This is due to the fact that when light irradiates the sensor, the trapped electrons in the material are activated, increasing the material's conductivity. It can be seen from the figure that the sensor produces strong photoconductivity effect under the irradiation of 325 nm wavelength laser and slightly weak photoconductivity effect under the irradiation of 442 nm wavelength laser. The real-time photocurrents of the sensor under optical switching (illumination conditions: laser wavelengths of 325 nm and 442 nm wavelengths, respectively) are shown in Fig. 5(b) and (c), respectively. The bias voltage of the device is 2.0 V. The sensor exhibited an optical on/off current ratio of 18 when irradiated with a 325 nm wavelength laser and 3.3 when irradiated with a 442 nm wavelength laser. The optical conductivity of the sensor increases gradually after light irradiation, and the response times of the 325 nm and 442 nm lasers are 25 s and 18 s, respectively. After turning off the light, the optical conductivity gradually decreases, the recovery time is 13 s and 12 s, and there is relaxation. It has good stability and can be used in the field of photoconductive switches.

The gas sensors based on the ZC1, ZC2, ZC3, ZC4, and ZC0 will be tested by CGS-MT, respectively. The bias voltage is also 2.0 V and test the corresponding strength of ZC1–ZC4 and ZC0 to 200 ppm normal butanol at the operating temperature of 160–400 °C. Response (S) refers to the sensor's response strength to the gas to be measured, which is defined as: $S = R_a/R_g$, where R_a is the sensor's resistance in air and R_g is the sensor's resistance in the gas to be measured. As shown in Fig. 6(a), ZC2 is the most sensitive to normal butanol gas. Normal butanol gas needs to react with the oxygen ion on the sensor surface at a suitable temperature to improve the activation energy. The chemical activation of sensing materials by test gas is minimal at lower temperatures, producing a very minimal response. While the adsorbed gas molecules would escape before their reaction if the operating temperature were too high due to their higher activation, which would decrease the response proportionally. The response to gas response reaches a maximum of 151.8 when ZC2 is at 300 °C. Under the same conditions, the optimal working temperature of the ZC0 is 400 °C, and the response is 6.47. At the optimum temperature, the response and recovery diagram of normal butanol gas with sensor degree of 200 ppm is shown in Fig. 6(b) and (c). The response intensity of the ZC2 sensor to normal butanol gas is approximately 151.8, with response and recovery times of 23 s and 10 s, respectively. The response strength of the ZC2 sensor is increased by 23.5 times when compared to the ZC0 sensor, and the optimal operating temperature is reduced by 100 °C, which is more energy-saving in practical production applications. The experiment shows that doping Co and Mn can significantly improve ZnO sensor response, and the gas sensor

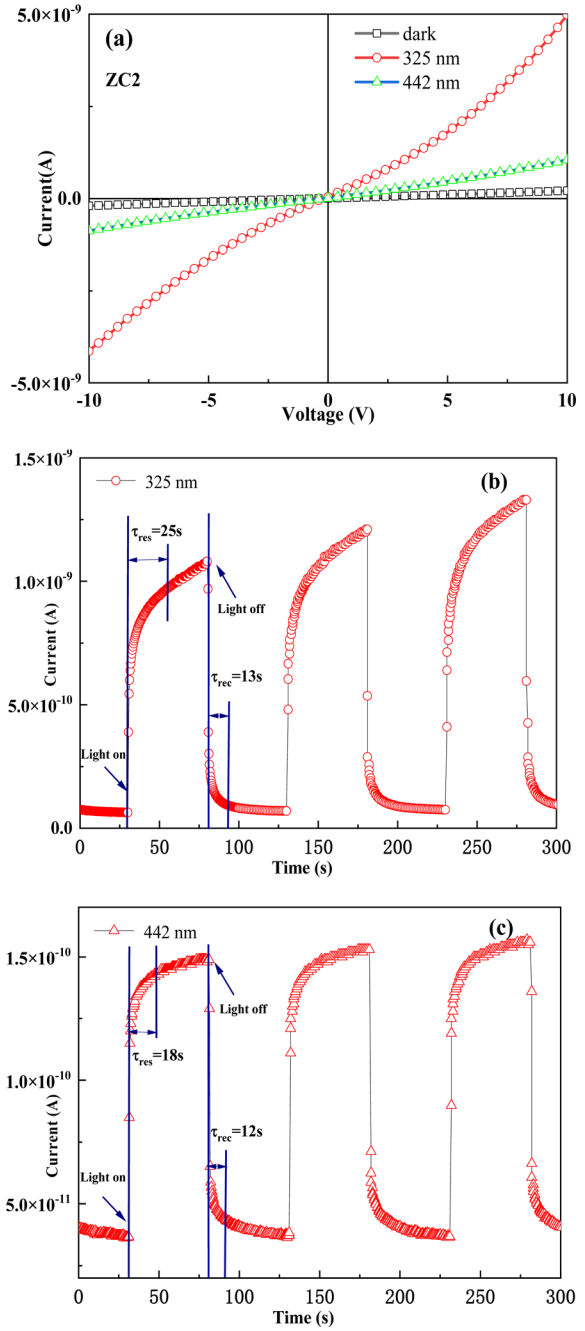

Fig. 5 (a) The *I*–*V* curves of the sensor based on the ZC2 under different illumination conditions: dark, 325 nm, and 442 nm wavelength of laser, respectively. (b) Under a 2 V bias, the real-time photocurrent curves (*I*–*t*) of the sensor based on the ZC2 under the light switching on and off (325 nm wavelength of laser). (c) Under a 2 V bias, the real-time photocurrent curves (*I*–*t*) of the sensor based on the ZC2 under the light switching on and off (442 nm wavelength of laser).

has reversible response to normal butanol gas with high response intensity and fast response recovery.[36] Fig. 6(d) and (e) depicts the response–recovery diagram of four-cycle tests performed at 300 °C and 200 ppm normal butanol gas. It can be concluded that the sensor has good stability and can quickly return to its initial value.

The relationship between the sensitivity (S) of the gas sensor and the concentration (C) of normal butanol gas can be described by a specific formula:

$$S = 1 + K\cdot[C]^{\beta} \quad (3)$$

In formula (3), S represents the sensitivity of the gas sensor, C represents the concentration of *n*-butanol gas (ppm), K represents the rate constant of the gas–solid reaction, and its reciprocal ($K^{-1} = [C]$) represents the sensitivity threshold of the sensor to normal butanol gas. β is a constant related to the type of oxygen ion, which can be determined by the slope of the relationship between the sensitivity of the sensor and the concentration of normal butanol under double logarithmic coordinates.

We tested the response values of the ZC2 sensor at normal butanol concentrations of 50 ppm, 100 ppm, 200 ppm, 300 ppm, 400 ppm, 600 ppm, 800 ppm, and 1000 ppm, as shown in Fig. 6(f). By performing double logarithmic linear fitting on the experimental data, we can further test the detection limit of the sensor. Because S-1 should ideally be greater than 1, further extrapolating the fitting curve to $S = 3$, we can obtain the detection limit of sensor ZC2 for *n*-butanol gas. By calculation, the detection limit of sensor ZC2 is found to be 10.2 ppm. This result further demonstrates the superiority of the ZC2 sensor in the field of low-concentration gas detection.

According to the literature, Zou *et al.*'s research group synthesized ZnO nanocrystals using a low-temperature solvent thermal method.[37] At the optimal operating temperature of 340 °C, their sensor exhibited a response of 145 to 500 ppm *n*-butanol. In contrast, our ZC2 sensor showed improved performance, with the optimal operating temperature being 300 °C. At this temperature, the sensitivity reached 151.8 even at a lower concentration of 200 ppm *n*-butanol gas.

The ZC2 gas sensor is exposed to 200 ppm of normal butanol, methanol, and acetone gases at 300 °C, respectively, to examine the selectivity of the sensor. The sensor's response to normal butanol gas is substantially higher than its responses to the other three VOCs gases (methanol, acetone, and ethanol), as seen in Fig. 7(a), demonstrating the sensor's strong selectivity for normal butanol gas. It can effectively detect the concentration of normal butanol gas in VOCs with high sensitivity.

We also conducted long-term stability tests on the ZC2 sensor. After storing it for 300 days, we tested its response to 200 ppm of *n*-butanol gas under the same experimental conditions. As shown in Fig. 7(b), the sensitivity of the annealed ZC2 sensor was 157.7. Compared to when it was first prepared, there was almost no change in sensitivity and response recovery time, demonstrating the ZC2 sensor's excellent long-term stability. As a result, the ZC2 sensor has high stability, repeatability, response strength, fast response, and fast recovery.

Bimetallic (Co, Mn) co-doped ZnO hierarchical nanostructures do not agglomerated, which is conducive to the rapid flow of gas molecules and sufficient contact with materials. During the reaction, (Co, Mn) co-doped ZnO hierarchical nanostructures continuously adsorb O_2 and react with it to produce O^{2-}, O_2^-, and O^-.[38,39] When the sensor is immersed in

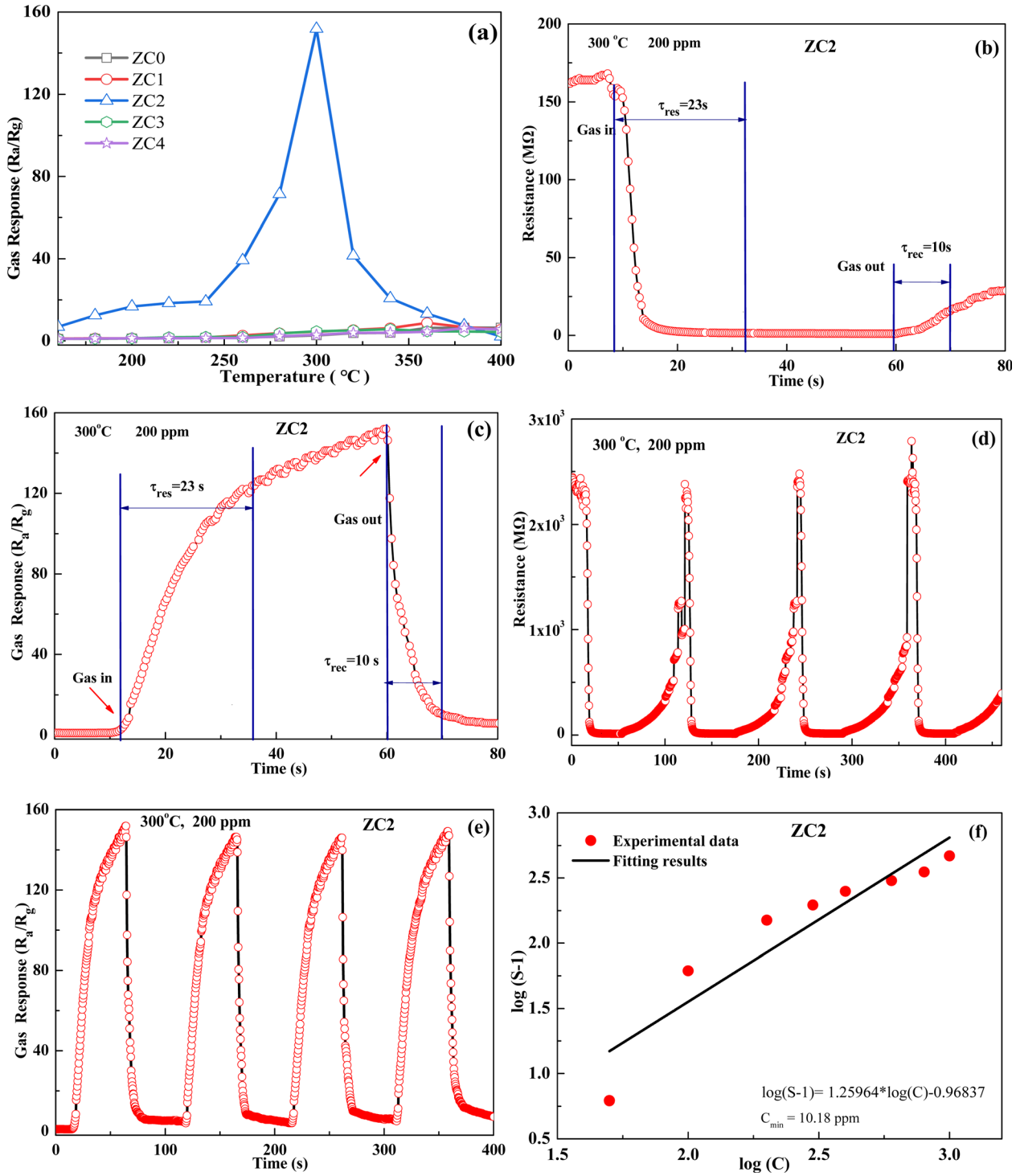

Fig. 6 (a) Response of the gas sensors based on the ZC1, ZC2, ZC3, ZC4, and ZC0 to 200 ppm normal butanol gas at different temperatures, respectively. (b) Resistance of ZC2-based gas sensor for response time (τ_{res}) and recovery time (τ_{rec}) to 200 ppm *n*-butanol gas at 300 °C. (c) Response of ZC2-based gas sensor for response time (τ_{res}) and recovery time (τ_{rec}) to 200 ppm *n*-butanol gas at 300 °C. (d) Resistance of ZC2-based gas sensor tested for stability to 200 ppm *n*-butanol gas at 300 °C. (e) Response of ZC2-based gas sensor tested for stability to 200 ppm *n*-butanol gas at 300 °C. (f) Response of ZC2-based gas sensor at an operating temperature of 300 °C with different concentrations of normal butanol gas.

normal butanol gas, normal butanol and oxygen ions on the material's surface undergo oxidation–reduction reactions. When the sensor is in a reducing gas such as normal butanol, the normal butanol gas has a redox reaction with the oxygen ions on the surface of the material, the concentration of oxygen ions decreases, the electron concentration increases, and the resistance decreases. The reaction equation is as follows:

$$O_2(gas) \leftrightarrow O_2(ads) \quad (4)$$

$$O_2(ads) + e^- \leftrightarrow O_2^-(ads) \quad (5)$$

$$O_2^-(ads) + e^- \leftrightarrow 2O^-(ads) \quad (6)$$

$$O^-(ads) + e^- \leftrightarrow O_2^-(ads) \quad (7)$$

$$12O^-(ads) + CH_3(CH_2)_3OH \rightarrow 4CO_2 + 5H_2O + 12e^- \quad (8)$$

$$12O_2^-(ads) + CH_3(CH_2)_3OH \rightarrow 4CO_2 + 5H_2O + 24e^- \quad (9)$$

The gas sensing mechanism of normal butanol gas adsorbed on the (Co, Mn) co-doped ZnO nanostructures surface is shown in Fig. 8(a). The conductivity of gas sensors is determined by the concentration of carriers and the mobility of electron–hole pairs. When the temperature rises, oxygen ions are adsorbed on the surface of ZnO, which reduces the electron concentration on the sensor surface and forms a high-resistance depletion layer. When the sensor is in the environment of normal butanol gas, the redox reaction between normal butanol gas and oxygen ions releases electrons, thereby reducing the resistance value of the sensor. The doping of transition metals will provide more active adsorption sites, which will adsorb normal butanol gas at a given temperature. Next, the sites of Co and Mn in the ZnO lattice may support the catalytic conversion of normal butanol gas to its oxidation products.[40,41] As a result, when compared to pure ZnO, the gas response of (Co, Mn) co-doped ZnO nanostructures is higher, indicating that Co and Mn doping provides more active adsorption sites. Bimetallic synergistic effect should play a leading role. Therefore, the mechanism of the promoted gas sensing performance would be attributed to the

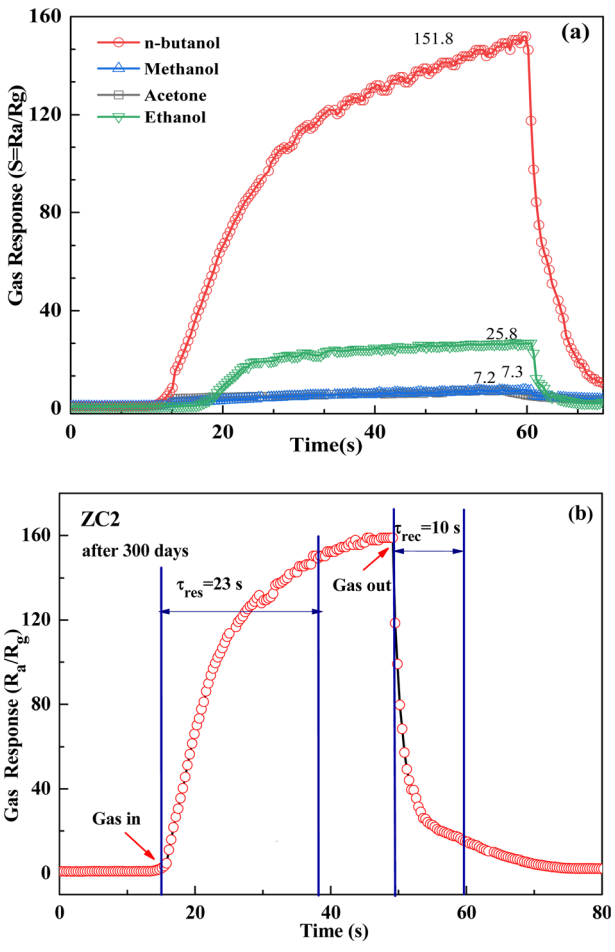

Fig. 7 (a) Response of ZC2-based gas sensor selective response to 200 ppm different gases (normal butanol, methanol, acetone, and ethanol, respectively) at 300 °C. (b) Resistance of ZC2-based gas sensor for response time (τ_{res}) and recovery time (τ_{rec}) to 200 ppm *n*-butanol gas at 300 °C after 450 days.

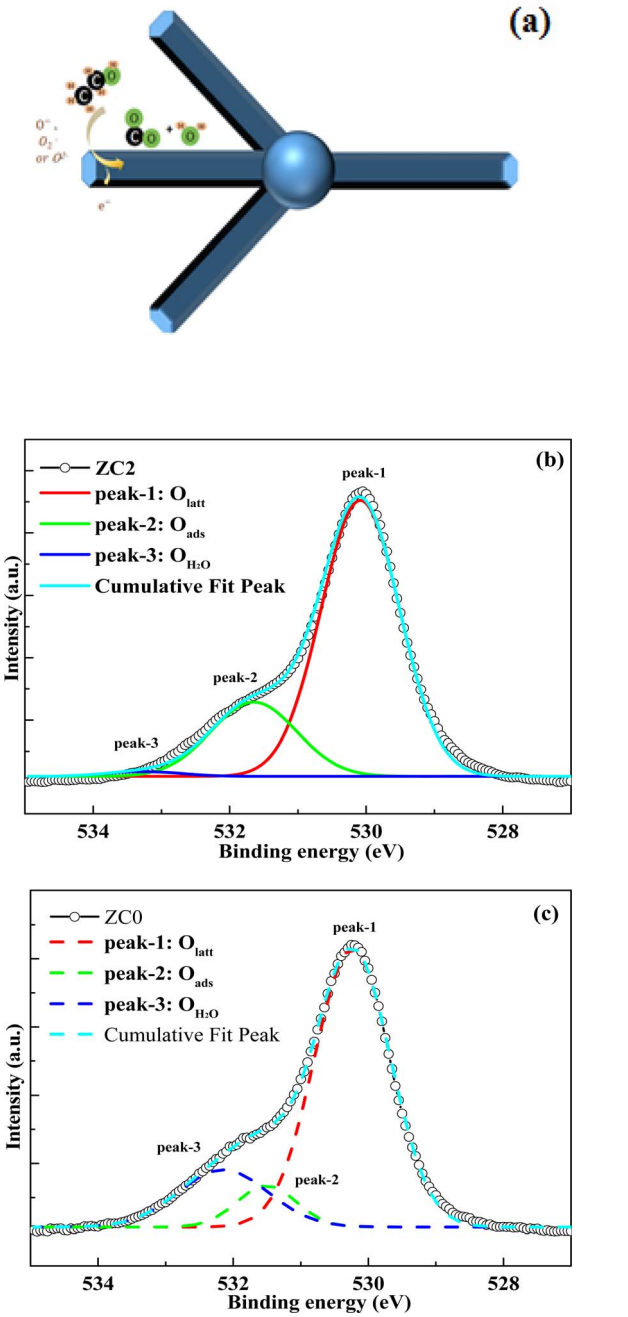

Fig. 8 (a) Diagram of the gas sensing mechanism. (b) O 1s multi-peak fitting curve of the sample ZC2. (c) O 1s multi-peak fitting curve of the sample ZC0.

Table 1 The contents of different oxygen species (O_{latt}, O_{ads}, and O_{H_2O}) in materials ZC1, ZC2, ZC3, ZC4 and ZC0

	O_{latt} (%)	O_{ads} (%)	O_{H_2O} (%)
ZC1	70.0	12	18
ZC2	76.3	22.4	1.3
ZC3	77.5	7.5	15
ZC4	75.8	8.4	15.8
ZC0	73.6	8.5	17.9

bimetallic synergistic enhancement effect. The interaction between Mn and Co sites not only affects the chemical coordination environment, but also promotes the activity of reduction reaction.

For resistor-type gas sensors such as ZC1–ZC4 and ZC0, the content of chemisorbed oxygen on the material surface plays a crucial role in determining its gas sensing performance. To provide support for the significance of chemisorbed oxygen on gas response, the multiple peak fitting of the O 1s XPS spectrum for the ZC2 sample is investigated and compared it with the XPS data of ZC0. As shown in Fig. 8(b), the O 1s spectrum of ZC2 was fitted into three distinct diffraction peaks. These peaks are associated with oxygen originating from the ZnO lattice (O_{latt}, peak-1), oxygen adsorbed onto the material from the ambient air (O_{ads}, peak-2), and oxygen adsorbed from water vapor in the air (O_{H_2O}, peak-3). Similarly, Fig. 8(c) depicts the O 1s spectrum of material ZC0, which was also fitted into three peaks corresponding to lattice oxygen, adsorbed oxygen, and water vapor oxygen. By calculating the peak areas, we determined the contents of different oxygen species in the materials, as summarized in Table 1. In material ZC2, the content of lattice oxygen was found to be 76.3%, adsorbed oxygen was 22.4%, and water vapor oxygen was 1.3%. For material ZC0, the content of lattice oxygen was 73.6%, adsorbed oxygen was 8.5%, and water vapor oxygen was 17.9%. A comparison reveals that the proportion of adsorbed oxygen in ZC2 is much higher than that of in ZC0. We also performed XPS measurements for ZC1, ZC3, and ZC4, and by comparing the results with ZC0, we found that ZC2 exhibits the highest content of adsorbed oxygen. By integrating these findings with the gas response test results, it becomes evident that the gas response of the materials increases with higher contents of adsorbed oxygen. The increase of adsorbed oxygen content can be attributed to the synergistic enhancement effect through the interaction between bimetallic (Co, Mn), which leads to electron enrichment on the material surfaces and helps to improve the gas sensing performance of sensors. The analyzed results of O 1s fractional peak in XPS spectra further confirm that the bimetallic synergistic effect can enrich electrons on the surface of materials. Electron enrichment on the surface of the material can not only enhance the activity of the material, but also improve the gas-sensing properties of the material.

4. Conclusion

In this paper, (Co, Mn) co-doped ZnO hierarchical nanostructures were prepared by controlling the doping ratio of Co and Mn. The structural properties, photoelectric properties and gas-sensing properties of the synthesized materials were studied and analyzed. The results showed that Co ions and Mn ions successfully replaced Zn ions during the doping process. PL spectra demonstrate that (Co, Mn) co-doped ZnO hierarchical nanostructures have higher crystallinity than pure ZnO. (Co, Mn) co-doped ZnO hierarchical nanostructures exhibit strong photoconductivity under different illumination conditions. The gas sensor based on the (Co, Mn) co-doped ZnO hierarchical nanostructures has a stronger response to normal butanol gas compared to a pure ZnO sensor and has high stability, high selectivity, good repeatability, a high response intensity, a quick reaction time, and other characteristics. The experimental results show that the optoelectronic and gas-sensing properties of (Co, Mn) co-doped ZnO hierarchical nanostructures can be significantly improved. The improvement of the sensor's performance is attributed to the increase of adsorbed oxygen content on the surface of the sensor material due to the bimetallic synergistic enhancement effect.

Data availability

The data that support the findings of this study are available from the corresponding author upon reasonable request.

Author contributions

Y. W. Q. synthesized the samples and performed the performance tests. J. Z. conceived the idea, coordinated all stages of this research, and supervised the work. Y. W. Q. and J. Z. wrote the manuscript. All authors contributed to the manuscript.

Conflicts of interest

The authors declare no competing interests.

Acknowledgements

This work was supported by the National Natural Science Foundation of China (Grant No. 60277023).

References

1 M. R. R. Khan, B. H. Kang, S. H. Yeom, *et al.*, Fiber-optic pulse width modulation sensor for low concentration VOC gas, *Sens. Actuators, B*, 2013, **188**, 689–696.
2 H. Wang, Y. Qu, H. Chen, *et al.*, Highly selective n-butanol gas sensor based on mesoporous SnO_2 prepared with hydrothermal treatment, *Sens. Actuators, B*, 2014, **201**, 153–159.
3 T. Gao and T. H. Wang, Synthesis and properties of multipod-shaped ZnO nanorods for gas-sensor applications, *Appl. Phys. A*, 2005, **80**, 1451–1454.
4 J. Xu, J. Han, Y. Zhang, *et al.*, Studies on alcohol sensing mechanism of ZnO based gas sensors, *Sens. Actuators, B*, 2008, **132**(1), 334–339.

5 M. Nirmala, P. Smitha and A. Anukaliani, Optical and electrical properties of undoped and (Mn, Co) co-doped ZnO nanoparticles synthesized by DC thermal plasma method, *Superlattices Microstruct.*, 2011, **50**(5), 563–571.
6 J. Xu, Y. Zhang, Y. Chen, *et al.*, Uniform ZnO nanorods can be used to improve the response of ZnO gas sensor, *Mater. Sci. Eng. B*, 2008, **150**(1), 55–60.
7 C. N. Wang, Y. L. Li, F. L. Gong, *et al.*, Advances in doped ZnO nanostructures for gas sensor, *Chem. Rec.*, 2020, **20**(12), 1553–1567.
8 M. Miki-Yoshida, J. Morales and J. Solis, Influence of Al, In, Cu, Fe and Sn dopants on the response of thin film ZnO gas sensor to normal butanol vapour, *Thin Solid Films*, 2000, **373**(1–2), 137–140.
9 Y. Fan, Y. Xu, Y. Wang, *et al.*, Fabrication and characterization of Co-doped ZnO nanodiscs for selective TEA sensor applications with high response, high selectivity and ppb-level detection limit, *J. Alloys Compd.*, 2021, **876**, 160170.
10 R. Khan, S. Fashu, Z. U. Rehman, *et al.*, Structure and magnetic properties of (Co, Mn) co-doped ZnO diluted magnetic semiconductor nanoparticles, *J. Mater. Sci.: Mater. Electron.*, 2018, **29**, 32–37.
11 P. Pascariu, I. V. Tudose, M. Suchea, *et al.*, Preparation and characterization of Ni, Co doped ZnO nanoparticles for photocatalytic applications, *Appl. Surf. Sci.*, 2018, **448**, 481–488.
12 R. Khan, C. I. Levartoski de Araujo, T. Khan, *et al.*, Influence of oxygen vacancies on the structural, dielectric, and magnetic properties of (Mn, Co) co-doped ZnO nanostructures, *J. Mater. Sci.: Mater. Electron.*, 2018, **29**, 9785–9795.
13 M. Zubair, A. Khan, T. Hua, *et al.*, Oxygen vacancies induced room temperature ferromagnetism and enhanced dielectric properties in Co and Mn co-doped ZnO nanoparticles, *J. Mater. Sci.: Mater. Electron.*, 2021, **32**, 9463–9474.
14 B. Poornaprakash, U. Chalapathi, S. Babu, *et al.*, Structural, morphological, optical, and magnetic properties of Gd-doped and (Gd, Mn) co-doped ZnO nanoparticles, *Phys. E*, 2017, **93**, 111–115.
15 S. Aksoy, Y. Caglar, S. Ilican, *et al.*, Sol-gel derived Li-Mg co-doped ZnO films: preparation and characterization via XRD, XPS, FESEM, *J. Alloys Compd.*, 2012, **512**(1), 171–178.
16 J. L. Van Heerden and R. Swanepoel, XRD analysis of ZnO thin films prepared by spray pyrolysis, *Thin Solid Films*, 1997, **299**(1–2), 72–77.
17 H. Savaloni and R. Savari, Nano-structural variations of ZnO: N thin films as a function of deposition angle and annealing conditions: XRD, AFM, FESEM and EDS analyses, *Mater. Chem. Phys.*, 2018, **214**, 402–420.
18 Z. K. Heiba and L. Arda, XRD, XPS, optical, and Raman investigations of structural changes of nano Co-doped ZnO, *J. Mol. Struct.*, 2012, **1022**, 167–171.
19 H. S. Al-Salman and M. J. Abdullah, Structural, optical, and electrical properties of Schottky diodes based on undoped and cobalt-doped ZnO nanorods prepared by RF-magnetron sputtering, *Mater. Sci. Eng., B*, 2013, **178**, 1048.
20 J. Mohapatra, D. K. Mishra, D. Mishra, *et al.*, Room temperature ferromagnetism in Co doped ZnO within an optimal doping level of 5%, *Mater. Res. Bull.*, 2012, **47**(6), 1417–1422.
21 L. Yan, C. K. Ong and X. S. Rao, Magnetic order in Co-doped and (Mn, Co) co-doped ZnO thin films by pulsed laser deposition, *J. Appl. Phys.*, 2004, **96**(1), 508–511.
22 R. D. Shannon, Revised effective ionic radii and systematic studies of interatomic distances in halides and chalcogenides, *Acta Crystallogr., Sect. A: Cryst. Phys., Diffr., Theor. Gen. Crystallogr.*, 1976, **32**(5), 751–767.
23 B. Yahmadi, O. Kamoun, B. Alhalaili, *et al.*, Physical investigations of (Co, Mn) Co-doped ZnO nanocrystalline films, *Nanomaterials*, 2020, **10**(8), 1507.
24 N. Ahmad, S. Khan and M. M. N. Ansari, Exploration of Raman spectroscopy, dielectric and magnetic properties of (Mn, Co) co-doped SnO_2 nanoparticles, *Phys. B*, 2019, **558**, 131–141.
25 X. Xue, W. Ruan, L. Yang, *et al.*, Surface-enhanced Raman scattering of molecules adsorbed on Co-doped ZnO nanoparticles, *J. Raman Spectrosc.*, 2012, **43**(1), 61–64.
26 R. D. Shannon, Revised effective ionic radii and systematic studies of interatomic distances in halides and chalcogenides, *Acta Crystallogr., Sect. A: Cryst. Phys., Diffr., Theor. Gen. Crystallogr.*, 1976, **32**(5), 751–767.
27 T. J. Chuang, C. R. Brundle and D. W. Rice, Interpretation of the x-ray photoemission spectra of cobalt oxides and cobalt oxide surfaces, *Surf. Sci.*, 1976, **59**(2), 413–429.
28 C. Yu, X. Guan, G. Li, *et al.*, A novel approach to composite electrode $0.3Li_2MnO_{3-0.7}LiMn_{1/3}Ni_{1/3}Co_{1/3}O_2$ in lithium-ion batteries with an anomalous capacity and cycling stability at 45.4 °C, *Scr. Mater.*, 2012, **66**(5), 300–303.
29 Q. Li, G. Li, C. Fu, *et al.*, Balancing stability and specific energy in Li-rich cathodes for lithium ion batteries: a case study of a novel Li-Mn-Ni-Co oxide, *J. Mater. Chem. A*, 2015, **3**(19), 10592–10602.
30 C. Fu, G. Li, D. Luo, *et al.*, Gel-combustion synthesis of $Li_{1.2}Mn_{0.4}Co_{0.4}O_2$ composites with a high capacity and superior rate capability for lithium-ion batteries, *J. Mater. Chem. A*, 2014, **2**(5), 1471–1483.
31 S. Ivanova, E. Zhecheva, R. Stoyanova, *et al.*, High-voltage $LiNi_{1/2}Mn_{3/2}O_4$ spinel: cationic order and particle size distribution, *J. Phys. Chem. C*, 2011, **115**(50), 25170–25182.
32 Y. Xiao, S. Ge, L. Xi, *et al.*, Room temperature ferromagnetism of Mn-doped SnO_2 thin films fabricated by sol-gel method, *Appl. Surf. Sci.*, 2008, **254**(22), 7459–7463.
33 G. Demircan, S. Yalcin, K. Alivi, *et al.*, The effect of Co and Mn co-doping on structural and optical properties of ZnO thin films, *Opt. Mater.*, 2022, **126**, 112163.
34 A. B. Djurišić, W. C. H. Choy, V. A. L. Roy, *et al.*, Photoluminescence and electron paramagnetic resonance of ZnO tetrapod structures, *Adv. Funct. Mater.*, 2004, **14**(9), 856–864.
35 S. K. Jesudoss, J. J. Vijaya, N. C. S. Selvam, *et al.*, Effects of Ba doping on structural, morphological, optical, and photocatalytic properties of self-assembled ZnO

nanospheres, *Clean Technol. Environ. Policy*, 2016, **18**, 729–741.

36 Z. Pan, F. Sun, X. Zhu, *et al.*, Electrodeposition-based in situ construction of a ZnO-ordered macroporous film gas sensor with enhanced response, *J. Mater. Chem. A*, 2019, **7**(3), 1287–1299.

37 T. Zou, R. Zhao, Z. Wang, *et al.*, Sensitive and selective n-butanol gas detection based on ZnO nanocrystalline synthesized by a low-temperature solvothermal method, *Phys. E*, 2018, **103**, 143–150.

38 I. S. Hwang and J. H. Lee, Gas sensors using oxide nanowire networks: an overview, *J. Nanoeng. Nanomanuf.*, 2011, **1**(1), 4–17.

39 P. P. Sahay, Zinc oxide thin film gas sensor for detection of acetone, *J. Mater. Sci.*, 2005, **40**(16), 4383–4385.

40 J. Xu, S. Li, L. Li, *et al.*, Facile fabrication and superior gas sensing properties of sponge-like Co-doped ZnO microspheres for normal butanol sensors, *Ceram. Int.*, 2018, **44**(14), 16773–16780.

41 X. Liu, N. Chen, X. Xing, *et al.*, A high-performance n-butanol gas sensor based on ZnO nanoparticles synthesized by a low-temperature solvothermal route, *RSC Adv.*, 2015, **5**(67), 54372–54378.